



OPEN

Unveiling the local structure of the amorphous metal $\text{Fe}_{(1-x)}\text{Zr}_x$ combining first-principles-based simulations and modelling of EXAFS spectra

Giuseppe Muscas^{1,2}, Robert Johansson^{1,5}, Sebastian George¹, Martina Ahlberg^{1,3}, Dimitri Arvanitis¹, Rajeev Ahuja^{1,4}, Ralph H. Scheicher¹ & Petra E. Jönsson¹✉

Amorphous alloys exhibit useful properties such as the excellent soft magnetic behaviour of Fe-based metallic glasses. The detailed structure of amorphous $\text{Fe}_{(1-x)}\text{Zr}_x$ with $x = 0.07, 0.10, \text{ and } 0.20$ is in this work explored through a synergetic combination of atomistic simulations and experimental characterisation. Thin-film samples were investigated using X-ray diffraction and extended X-ray absorption fine structure (EXAFS), while the corresponding atomic structures were simulated using an efficient first-principles-based method called stochastic quenching (SQ). The simulated local atomic arrangements are investigated by constructing the radial- and angular-distribution functions, as well as by Voronoi tessellation. The radial distribution functions are then used to construct a model to fit simultaneously the experimental EXAFS data of multiple samples with different compositions, creating a simple yet accurate description of the atomic structures valid for any composition in the range $x = 0.07$ to 0.20 , using a minimal number of free parameters. This approach significantly improves the accuracy of the fitted parameters and allows us to relate the compositional dependence of the amorphous structures with the magnetic properties. The proposed EXAFS fitting process can be generalised to other amorphous systems, contributing to the understanding of structure-property relationships and the development of amorphous alloys with tailored functional properties.

The magnetic, electrical, and mechanical properties of any material stem from its atomic structure. While a crystalline structure can be completely described by a crystal class and lattice constants, this is not possible for a non-crystalline material, which thus has to be described and characterised in other ways^{1,2}. An amorphous material exhibits short-range order and long-range disorder^{3–6}. The structure of amorphous materials can be simulated by the stochastic quenching (SQ) method^{7–9}, or by the more computationally demanding molecular dynamics simulation method¹⁰. Simulated amorphous structures have been intensively investigated with focus on the radial distribution function (RDF) and the three-dimensional arrangement of atoms^{11–15}. The splitting of the second visible peak in the RDF is a characteristic feature of amorphous metals and it has been explained by considering the next-nearest-neighbour atomic arrangement^{1,11–13,15,16}. Recently, it has been attributed to the local quasi-icosahedral ordering in amorphous metals with the first sub-peak of the second peak originating from next-nearest-neighbour atoms with a three-atoms connection of the atomic clusters and the second sub-peak of the second peak originating from next-nearest-neighbour atoms with a one-atom connection of the atomic clusters^{12,13}. An accurate and valid atomic structure is a prerequisite for meaningful first-principles modelling of other physical properties. Extended X-ray absorption fine structure (EXAFS) data are sensitive to the short-range order and have been used to qualitatively validate simulated amorphous structures for a few amorphous alloys^{9,17,18}. Many details of the atomic structure of amorphous systems are however still unknown.

¹Department of Physics & Astronomy, Uppsala University, Box 516, 751 20 Uppsala, Sweden. ²Department of Physics, University of Cagliari, Cittadella Universitaria di Monserrato, S.P. 8 Km 0.700, 09042 Monserrato, CA, Italy. ³Department of Physics, University of Gothenburg, Fysikgränd 3, 412 96 Gothenburg, Sweden. ⁴Indian Institute of Technology Ropar, Rupnagar, Punjab 140001, India. ⁵Present address: Uppsala Clinical Research Center, Uppsala University Hospital, Box 6363, 751 35 Uppsala, Sweden. ✉email: petra.jonsson@physics.uu.se

Metallic glasses are an important class of amorphous materials because of their mechanical and soft-magnetic properties¹⁹. For magnetic metallic glasses, the Bethe-Slater curve models how the magnetic exchange energy depends on the interatomic distances and thereby provides basic insight into how the magnetic properties depend on the atomic structure²⁰. In particular for Fe-based compounds, the magnetic exchange energy depends strongly on the interatomic Fe-Fe distances and the Curie temperature therefore exhibits a strong pressure dependence²¹. Amorphous $\text{Fe}_{(1-x)}\text{Zr}_x$ has been studied extensively as a model system for amorphous iron^{22–30}. The magnetic properties have been shown to vary in a nontrivial manner with the chemical composition; for low Zr concentrations ($x \lesssim 0.2$) the Curie temperature increases with increasing Zr content while for higher Zr concentrations it decreases^{22,28}. For $\text{Fe}_{(1-x)}\text{Zr}_x$ samples with $x \approx 0.4–0.6$, the magnetic properties are strongly affected by the detailed synthesis conditions, and the observed variations in magnetic properties have been attributed to variations in the number of Fe-Fe nearest-neighbours^{23,29,30}. For samples prepared by melt-spinning with $x \approx 0.1$, neutron scattering experiments indicate the existence of magnetic inhomogeneities in form of clusters within the ferromagnetic matrix²⁷. Still, the amorphous ferromagnetic transition temperature is only slightly affected by structural inhomogeneities such as nanocrystallites²⁶. With an optimised sputtering process, it is possible to produce $\text{Fe}_{(1-x)}\text{Zr}_x$ samples without any sign of nanocrystallisation³¹.

The aim of this work is to provide a detailed structural analysis of $\text{Fe}_{(1-x)}\text{Zr}_x$ ($x = 0.07, 0.10, \text{ and } 0.20$). At first, the simulated amorphous structures obtained by the computationally convenient Stochastic Quenching simulation method are analysed. The simulated structures are validated using EXAFS data measured on sputtered samples. To quantify the validation, an advanced fitting process able to pinpoint small differences between the simulated and sputtered amorphous structures is developed. The radial distribution functions obtained for the simulated structures are used to construct a model of the first coordination shell independent of chemical composition to perform the EXAFS fitting. This model can be used to simultaneously fit the experimental EXAFS data of all the samples under investigation, which significantly improves the accuracy and solidity of the EXAFS analysis while using as few fitting parameters as possible.

Methods

Experimental. Amorphous $\text{Fe}_{(1-x)}\text{Zr}_x$ samples were grown by DC magnetron sputtering. A $\text{Fe}_{0.93}\text{Zr}_{0.07}$ sample was deposited from a compound target and the details about the sample preparation are given in Ref.³². $\text{Fe}_{0.90}\text{Zr}_{0.10}$ and $\text{Fe}_{0.80}\text{Zr}_{0.20}$ samples were deposited via co-sputtering from individual Fe and Zr targets at room temperature on $3''$ Si (001) substrates. The substrates were annealed at 650°C for 30 min prior to deposition in order to clean the surface. The base pressure of the chamber was below 8×10^{-10} Torr, while the growth was conducted with an Ar gas (99.9999 % pure) pressure of 2×10^{-3} Torr and substrate rotation. To facilitate the growth of completely amorphous $\text{Fe}_{(1-x)}\text{Zr}_x$, a buffer layer of amorphous $\text{Al}_{0.70}\text{Zr}_{0.30}$ (5 nm thick) was used, as well as a capping layer of $\text{Al}_{0.70}\text{Zr}_{0.30}$ (4 nm thick) to protect the samples against oxidation³¹. The compositions were confirmed to be within ± 0.5 at.% of the nominal values by Rutherford backscattering spectrometry (RBS). The analysis of the RBS spectra was performed using the SIMNRA simulation software^{33,34}.

X-ray reflectivity (XRR) measurements were collected in the 2θ range $0.2–8.0^\circ$ with a Bruker D8 Da Vinci diffractometer. With the same instrument, grazing-incidence X-ray diffraction (GIXRD) patterns were collected in the 2θ range $10–80^\circ$, with an incident angle of 1° . The measured XRR patterns were fitted using the GenX simulation software³⁵, in order to determine the thicknesses of the individual layers as well as their number densities. The results are presented in Table 1 together with values of the number densities reported in the literature^{36,37}. The GIXRD data (Fig. S1 in the supplementary information) confirm the x-ray amorphous character of all the samples.

Extended X-ray absorption fine structure (EXAFS) measurements were carried out at 80 and 300 K, using X-ray synchrotron radiation at beamline I811 at MAX-lab (Lund, Sweden). The data was collected in fluorescence mode over the K edge of Fe using a Si(111) double-crystal monochromator and an energy-dispersive solid-state detector (Si Nano Technology Vortex with a resolution $\Delta E/E$ of the order 10^{-4}). The data was obtained by averaging eight 40-minute scans per sample to improve the signal-to-noise ratio. The normalised EXAFS functions $\chi(k)$ were extracted from the raw data following standard procedures using the ATHENA software³⁸. Hanning windows are used for the Fourier transform with $k \sim 2.4–10.7 \text{ \AA}^{-1}$ for the amorphous samples and $2.4–12.5 \text{ \AA}^{-1}$ for the Fe film. Unfortunately, it was not possible to measure over the K-edge of Zr with enough accuracy due to experimental limitations. The measurements at 80 and 300 K did not significantly differ, except for the expected reduction of the thermal disorder and hence a slightly better signal-to-noise ratio in the low-temperature data. Therefore, the investigation was focused on the 80 K data.

Composition	Thickness (Å)	Number density, ρ_N (\AA^{-3})	
	XRR fit	XRR fit	Refs. ^{36,37}
$\text{Fe}_{0.93}\text{Zr}_{0.07}$	400(5)	0.080(2)	0.080
$\text{Fe}_{0.90}\text{Zr}_{0.10}$	999(5)	0.078(2)	0.078
$\text{Fe}_{0.80}\text{Zr}_{0.20}$	758(5)	0.070(3)	0.073

Table 1. The thicknesses and number densities obtained by fitting the XRR patterns using the GenX software³⁵. The number density values reported in the literature^{36,37} are also included.

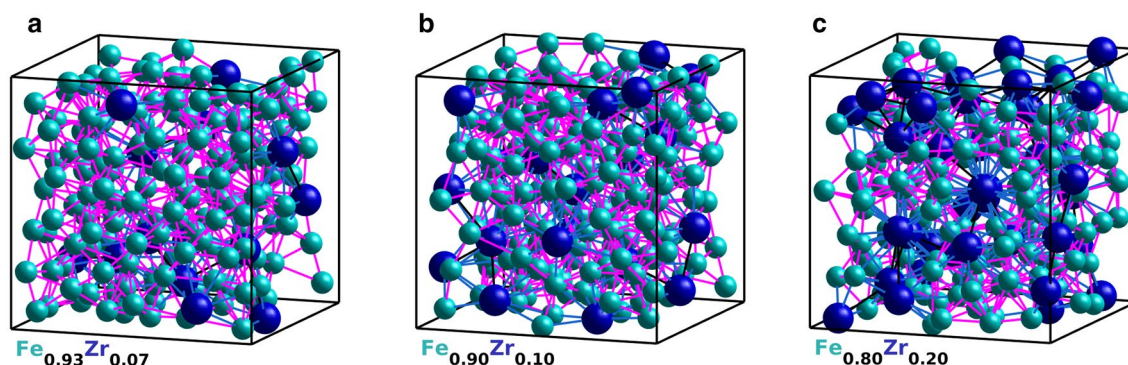


Figure 1. Illustration of the atomic arrangement in one of the simulated supercells for Fe_{0.93}Zr_{0.07}, Fe_{0.90}Zr_{0.10}, and Fe_{0.80}Zr_{0.20} from left to right. The larger dark blue spheres represent Zr atoms and the smaller cyan spheres represent Fe atoms. Nearest neighbour bounds are indicated by lines (magenta for Fe-Fe, blue for Fe-Zr, and black for Zr-Zr). The simulations used periodic boundary conditions.

Simulated amorphous structures. The simulated amorphous structures of Fe_(1-x)Zr_x ($x = 0.07, 0.10,$ and 0.20) were created using the SQ method⁷⁻⁹. The SQ method initiates from a random starting configuration of atoms and relaxes the positions of the atoms to the nearest local minimum in the potential-energy landscape. By repeatedly carrying out this process for a number of different random starting positions, we create samples of the amorphous structure, which are then subsequently used to obtain averages of the investigated properties. Due to the nature of the potential energy landscape, a structure which has been relaxed to the nearest local minimum from a random starting configuration is a good representation of an amorphous structure for the given composition of elements. The corresponding experimental sample would be one quenched from a melt with a very rapid cooling rate, or in the case of sputtering, be one with the kinetic energy of the adatoms perfectly tuned both to avoid any kind of clustering and to avoid porous growth.

The only experimental input to the simulations was the values of the number densities that were chosen according to the literature values reported in Table 1^{36,37}. The atoms are initially stochastically distributed into a cubic supercell with the only constraint being that the nearest-neighbour distance must be larger than a chosen minimum distance. The relaxation of the atomic structures to nearby energy minima was performed using the Vienna *Ab initio* Simulation Package (VASP)^{10,39-41}. The interactions between the electrons and the nuclei were obtained using the projector-augmented-wave method^{42,43}. The generalised gradient approximation (GGA) in the parametrisation of Perdew-Burke-Ernzerhof (PBE)^{44,45} approach was employed to approximate the exchange and correlation terms in the density functional theory (DFT) method^{46,47}. A conjugate gradient algorithm was used to relax the atomic nuclei positions to a local minimum in the total energy landscape. Due to the large size of the supercell, it was considered appropriate to sample the Γ -point only in the Brillouin zone. A plane-wave energy cutoff of 400 eV was used. Initially, the minimum nearest neighbour distance was 1.4 Å. Comparisons with structures generated from the relaxation of initial stochastic configurations with a constraint of 0.5 Å for the nearest neighbour minimum distance yielded no notable difference in structural properties while the constraint of 1.4 Å offered a substantial improvement in computational time. The amorphous Fe_(1-x)Zr_x structures were for each composition modelled by the atomic relaxation of at least 50 random starting configurations of supercells, each containing in total 200 atoms. The details about the supercells including their size are reported in Table S1 in the supplementary information.

Voronoi tessellation was performed using the Voro++ software package⁴⁸. The difference in size between the Fe and Zr atoms is taken into account when creating the Voronoi polyhedra. The Voronoi indices are presented in the form $\langle n_3, n_4, n_5, n_6 \rangle$ where n_i denotes the number of surfaces with i number of edges. $\sum_i n_i$ gives the Voronoi coordination number. Voronoi polyhedra surfaces with an area that comprises less than 1% of the total area of the polyhedra are disregarded.

Results

The simulated amorphous structures. Representative examples of the simulated amorphous structures, generated with periodic boundary conditions, are shown in Fig. 1 for one of the supercells of each composition. The partial radial distribution functions (RDF) were calculated for Fe-Fe, Fe-Zr, and Zr-Zr pairs from the atomic positions in each supercell and then averaged using all the simulated supercells. Each partial RDF, $g(r)$, is normalised so that $g(r \rightarrow \infty) = 1$, in order to be able to directly compare the partial RDFs from simulations with different compositions. Next, all the partial RDFs for the different compositions were parameterised by fitting a sum of N Gaussians

$$g(r) = \sum_i^N a_i n_i(r; R_i, \sigma_i), \quad n_i(r; R_i, \sigma_i) = \frac{1}{\sqrt{2\pi\sigma_i^2}} \exp\left(-\frac{(r-R_i)^2}{2\sigma_i^2}\right), \quad (1)$$

where a_i is the amplitude, R_i the peak position, and σ_i the standard deviation of the i th Gaussian n_i . A fit of $g_{\text{Fe-Fe}}(r)$ for Fe_{0.93}Zr_{0.07} is shown in Fig. 2. The fit is within the statistical uncertainty of the partial RDF for

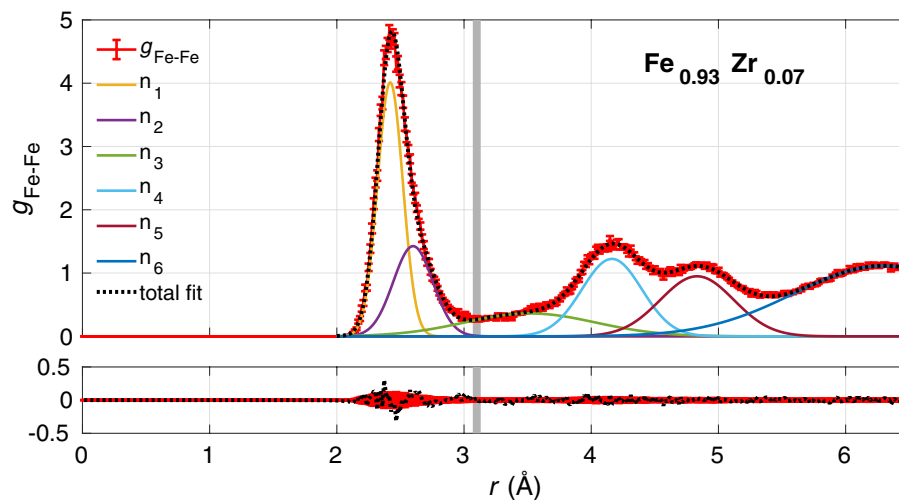


Figure 2. Partial radial distribution function for Fe-Fe pairs in $\text{Fe}_{0.93}\text{Zr}_{0.07}$. The lower panel shows the residual between the sum of the six Gaussians and $g_{\text{Fe-Fe}}(r)$ obtained from the simulated supercells. The gray vertical line indicates the limit of the first shell. In the lower panel, the difference between the total fit and $g_{\text{Fe-Fe}}$ are shown as black points while the standard deviation of the simulated partial radial distribution is indicated in red.

almost all values of r as can be seen in the lower panel of the figure. All partial RDFs for the three compositions were fitted and the peak positions of the first Gaussian, R_1 , are reported in Table 2. We note that all values of R_1 decrease with increasing Zr content, but, the relative positions of the other peaks are independent of composition for the simulated structures. To illustrate this, all partial RDFs are plotted versus r/R_1 in Fig. 3. At large r values, the RDFs flatten out due to the long-range disorder of the amorphous structures. A clear splitting of the second peak is seen for $g_{\text{Fe-Fe}}$ and $g_{\text{Fe-Zr}}$. A summary of the relative peak positions (R_i/R_1) obtained by fitting the Gaussians is reported in Table 3. Note that the R_4 and R_5 peaks are the first and second sub-peaks of the second visible peak of the RDF.

To further investigate the geometrical arrangement of atoms, the partial angular distribution functions (ADFs) were calculated from all $A-B-C$ atomic trios, where A and C are both within the nearest-neighbour shell around the central atom B . If each angle θ , defined as the angle between the $B-A$ and $B-C$ vectors, is equally probable due to a random arrangement of atoms, the probability distribution will exhibit a $\sin(\theta)$ dependence. Therefore, the probability at each angle θ is normalised by $\sin(\theta)^{-1}$ in order to give equal weight to each angle. The partial ADFs are shown in Fig. 4. With Fe as the central atom, the first peak is close to 60° for the Fe-Fe-Fe trios, indicating an equilateral triangular arrangement if only atoms of the same size are involved. If both Fe and Zr atoms are included, the angles deviate from 60° in accordance with larger Zr atoms and smaller Fe atoms. The minimum at 90° indicates that a cubic arrangement of atoms around Fe is unfavourable, while the additional peak in the A-Fe-C ADFs close to 117° is consistent with an icosahedral ordering of the atoms. It is only Fe-atoms surrounding Zr atoms that according to the Fe-Zr-Fe ADF have a tendency for cubic arrangements with peaks close to 45° , 90° , 135° and 180° . The first (lowest angle) peak in the A-B-C ADF contributes to the nearest-neighbor peak in g_{C-A} . For the A-Fe-Fe ADFs, it is the two atoms with an angle close to 117° to the central atom that give rise to the R_4 -peak in $g_{\text{Fe-A}}$ and those with an angle close to 180° that give rise to the R_5 -peak. The Zr-Zr-Zr ADF exhibits a minimum at 180° , indicating that Zr-atoms do not tend to form linear arrangements and explains the absence of R_5 -peak in $g_{\text{Zr-Zr}}$. A Voronoi analysis was performed to provide more information about the three-dimensional arrangement of the atoms. It revealed, in accordance with other metallic glasses⁶, a quasi-icosahedral ordering with typical Voronoi indices $(0, 1, 10, 2)$, $(0, 2, 8, 2)$, $(0, 3, 6, 4)$, and $(0, 0, 12, 0)$ for Fe atoms and $(0, 1, 10, 7)$ for Zr atoms.

	$R_1^{\text{Fe-Fe}}$ (Å)	$R_1^{\text{Fe-Zr}}$ (Å)	$R_1^{\text{Zr-Zr}}$ (Å)
$\text{Fe}_{0.93}\text{Zr}_{0.07}$	2.419(4)	2.79(3)	3.43(3)
$\text{Fe}_{0.90}\text{Zr}_{0.10}$	2.411(4)	2.78(2)	3.40(2)
$\text{Fe}_{0.80}\text{Zr}_{0.20}$	2.389(4)	2.73(2)	3.33(2)

Table 2. Peak positions of the first Gaussian, R_1 , obtained fitting Eq. (1) to the partial Fe-Fe, Fe-Zr, and Zr-Zr radial distribution functions for the simulated amorphous structures of $\text{Fe}_{0.93}\text{Zr}_{0.07}$, $\text{Fe}_{0.90}\text{Zr}_{0.10}$, and $\text{Fe}_{0.80}\text{Zr}_{0.20}$.

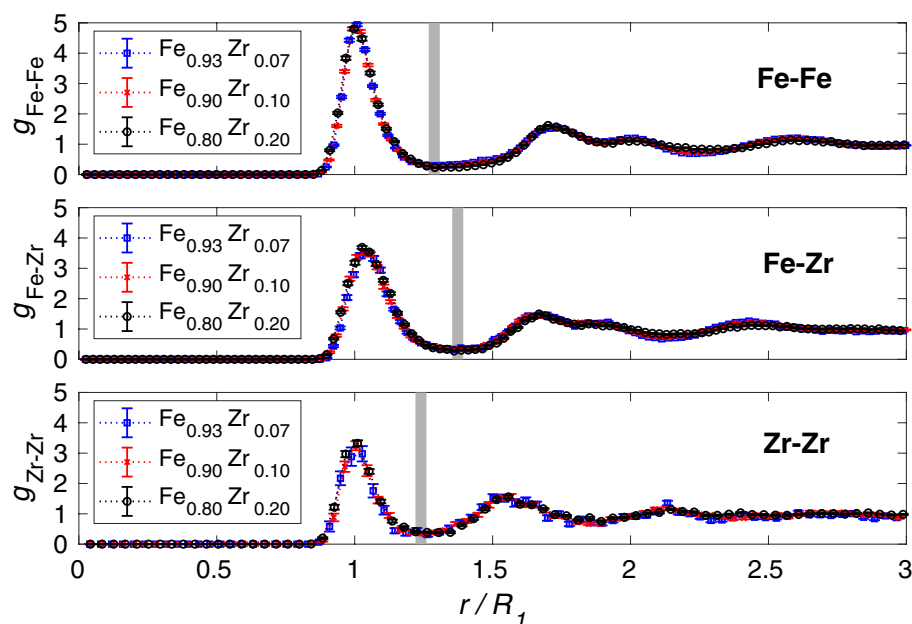


Figure 3. Partial radial distribution functions (RDFs) obtained from the simulated atomic positions for Fe-Fe, Fe-Zr, and Zr-Zr pairs versus r/R_1 . The R_1 values are reported in Table 2. The thick gray vertical lines indicate the limit of the first coordination shells.

	R_2/R_1	R_3/R_1	R_4/R_1	R_5/R_1
Fe-Fe	1.08(1)	1.46(4)	1.72(2)	2.00(2)
Fe-Zr	1.07(3)	1.2(1)	1.64(2)	1.82(2)
Zr-Zr	1.10(8)	–	1.56(4)	–

Table 3. Relative peak positions of the i th Gaussian obtained by fitting Eq. (1) to the partial Fe-Fe, Fe-Zr, and Zr-Zr radial distribution functions (RDF) for the simulated amorphous structures of $\text{Fe}_{0.93}\text{Zr}_{0.07}$, $\text{Fe}_{0.90}\text{Zr}_{0.10}$, and $\text{Fe}_{0.80}\text{Zr}_{0.20}$. For Fe-Fe and Fe-Zr, the R_4 and R_5 values are the peak positions of the first and second sub-peaks of the second visible peak of the partial RDFs. Fewer Gaussians are used to fit the Zr-Zr partial RDF and values for R_3 and R_5 are therefore missing so that the R_4 value is the peak position of the second visible peak in the Zr-Zr partial RDF.

EXAFS analysis. The k^2 -weighted Fe K-edge EXAFS signals, measured at 80 K, are shown in Fig. 5a for the amorphous $\text{Fe}_{(1-x)}\text{Zr}_x$ samples as well as for a crystalline BCC-Fe film as a reference. The magnitude of the Fourier transform of the $k^2 \chi(k)$ data are shown in Fig. 5b for the amorphous samples. The amplitude and accuracy of the $\chi(R)$ data beyond the first shell is very low and can not be included in any analysis.

In a first attempt to determine if the simulated atomic structures are compatible with the experimental EXAFS data, the average $\chi(q)$ function was calculated, using the FEFF8.50-Lite code^{49,50}, from the exact atomic positions in all supercells. Only atoms within the nearest-neighbour shell around each Fe atom were included in the calculation and periodic boundary conditions were applied. The amplitude S_0^2 and the energy shift ΔE_0 were fitted to the experimental data simultaneously for k -weights of 1, 2, and 3. The simulated and experimental $k^2 \chi(q)$ data are shown in Fig. S2 in the Supplementary Information. They are quite similar for $\text{Fe}_{0.93}\text{Zr}_{0.07}$ and $\text{Fe}_{0.90}\text{Zr}_{0.10}$, but clearly deviate for $\text{Fe}_{0.80}\text{Zr}_{0.20}$. We repeated the SQ simulation with a slightly lower number density for $\text{Fe}_{0.80}\text{Zr}_{0.20}$ (close to that obtained in the fit of the XRR data reported in Table 1). However, the simulated EXAFS signal was only slightly changed and the fit to the experimental data was not improved. Hence, an incorrect density in the simulation is not the reason for the discrepancy between the simulated and experimental EXAFS signal for the $\text{Fe}_{0.80}\text{Zr}_{0.20}$ sample.

In order to understand the differences between the simulated amorphous structures and those of the experimental samples, we have created a model to fit to the experimental EXAFS data for all samples. This model is based on the simulated partial Fe-Fe and Fe-Zr RDFs and uses the observation in Fig. 3 that the scaled partial RDFs are the same for all three compositions. Parameters from the Gaussian fits with $i = 1$ and 2 in Eq. (2) for $g_{\text{Fe-Fe}}$ and $g_{\text{Fe-Zr}}$ were used to construct the model consisting of 4 paths in total. The partial coordination number of each path is given by

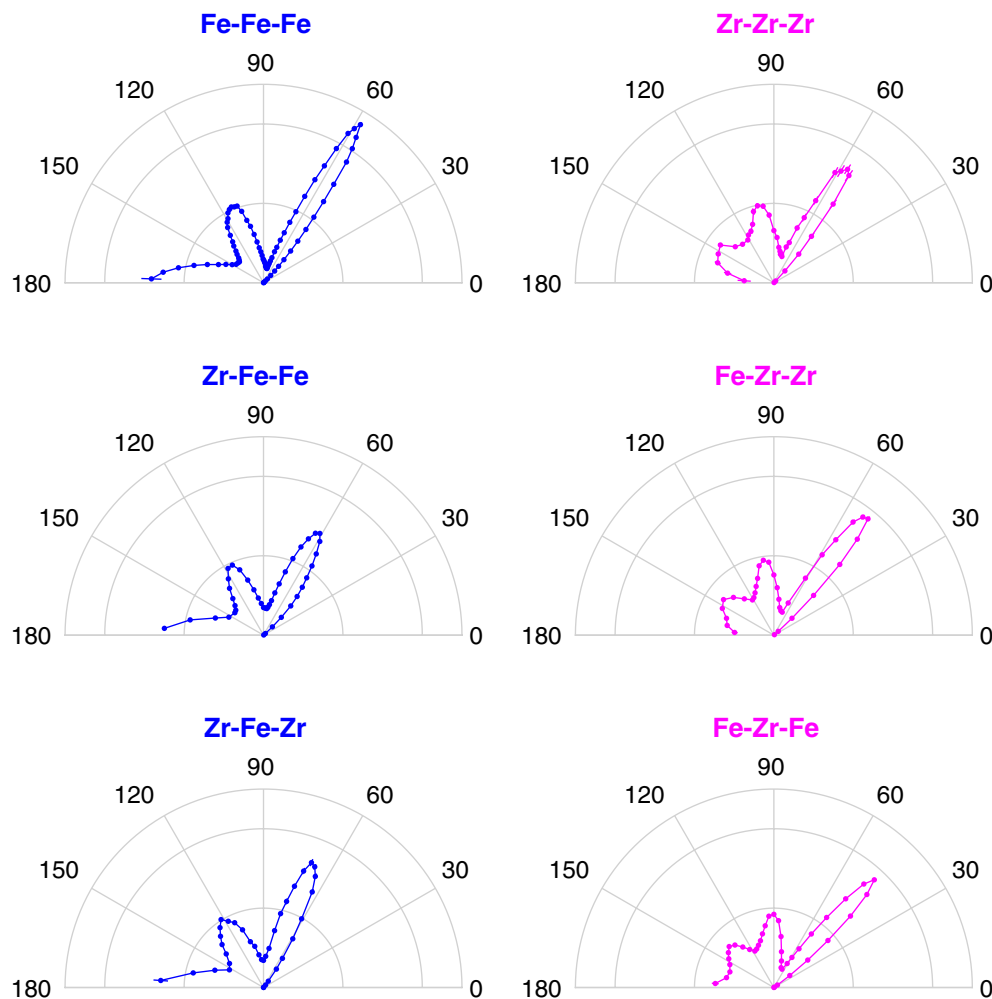


Figure 4. Polar plots of the partial angular distribution functions obtained from the simulated atomic positions for atoms belonging to the first shell around the central atom. These plots look quite similar for all compositions, but are only shown here for $\text{Fe}_{0.80}\text{Zr}_{0.20}$ due to the better statistics for Zr in that case. Error bars are plotted, but are generally smaller than the size of the data points. The position of the cut-off for the first shell is indicated as a gray line for each partial radial distribution function in Fig. 3.

$$N_i^{A-B} = 4\pi c_B \rho_N a_i \int_0^\infty \frac{r^2}{\sqrt{2\pi\sigma_i^2}} \exp\left(-\frac{(r-R_i)^2}{2\sigma_i^2}\right) dr = 4\pi \rho_B a_i (\sigma_i^2 + R_i^2). \quad (2)$$

where $\rho_B = c_B \rho_N$, c_B is the atomic content of element B, and ρ_N is the number density that is given in Table S1 (Supplementary Information) for the three compositions. a_i is the amplitude, R_i the peak position, and σ_i the standard deviation of the i th Gaussian ($i = 1$ or 2) according to Eq. (1). In order to further reduce the number of fitting parameters, the scaled Debye-Waller factors are assumed to be the same for the Fe-Fe and Fe-Zr paths of the same order, since the fitted values indicate that they are very similar. In the model, the scaled Fe-Fe and Fe-Zr coordination numbers are fixed to the values obtained by the Gaussian fits. The EXAFS $\chi(q)$ data belonging to the first shell were fitted simultaneously for all three samples using the ARTEMIS software package with a simultaneous k -weight of 1, 2, and 3, with some fitting variables in common for the three compositions. The values of all parameters that were fitted separately for the three $\text{Fe}_{(1-x)}\text{Zr}_x$ compositions are reported in Table 4 together with those obtained fitting a BCC structure to the Fe reference film. The values of the scaled parameters in the four EXAFS paths that are common for all samples are reported in Table 5 together with the corresponding values obtained for the two first Gaussians, when fitting $g_{\text{Fe-Fe}}$ and $g_{\text{Fe-Zr}}$ of the simulated structures to Eq. (1). The k^2 -weighted $|\chi(q)|$ data and the fits are shown in Fig. 6 for the three FeZr samples.

The main part of the EXAFS signal comes from Fe-Fe contributions and only a minor part from Fe-Zr contributions. Still, the Fe-Zr paths are needed in order to obtain good fits, though the parameter values from the Fe-Zr paths have higher uncertainty than those from the Fe-Fe paths. For the $\text{Fe}_{0.80}\text{Zr}_{0.20}$ sample, with the largest contribution from the Fe-Zr paths, $R_1^{\text{Fe-Zr}}$ was included as a fitting parameter and found within the uncertainties to be the same as the simulated value reported in Table 2. For the $\text{Fe}_{0.93}\text{Zr}_{0.07}$ and $\text{Fe}_{0.90}\text{Zr}_{0.10}$ samples, with

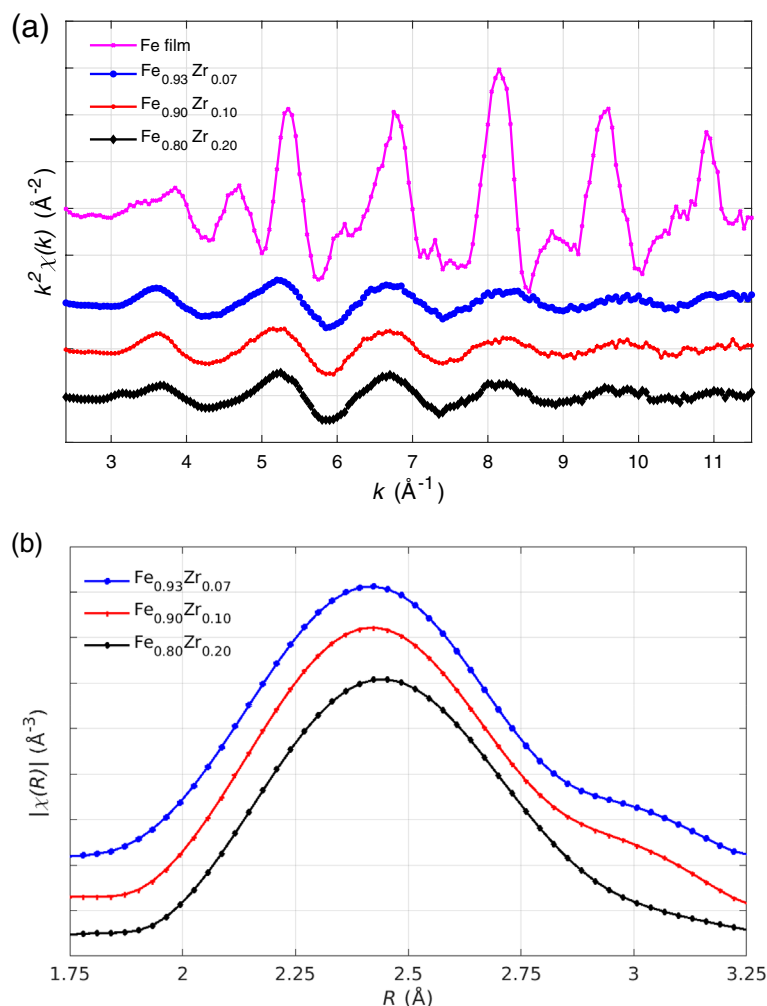


Figure 5. (a) EXAFS signal $k^2\chi$ measured at 80 K for $\text{Fe}_{0.93}\text{Zr}_{0.07}$, $\text{Fe}_{0.90}\text{Zr}_{0.10}$, $\text{Fe}_{0.80}\text{Zr}_{0.20}$, and the reference crystalline BCC-Fe film. (b) Its Fourier transform plotted with phase-correction for the three amorphous samples. All data are shifted vertically for clarity with the zero levels indicated by the grid.

	$R_1^{\text{Fe-Fe}}$ (\AA)	$R_1^{\text{Fe-Zr}}$ (\AA)	S_0^2	ΔE_0 (eV)
$\text{Fe}_{0.93}\text{Zr}_{0.07}$	2.432(8)	2.79	0.54(7)	4(2)
$\text{Fe}_{0.90}\text{Zr}_{0.10}$	2.440(7)	2.78	0.58(7)	4(2)
$\text{Fe}_{0.80}\text{Zr}_{0.20}$	2.442(8)	2.75(3)	0.60(7)	5(1)
Fe (BCC)	2.481(5)	–	0.7(1)	6(1)

Table 4. The parameter values obtained from the EXAFS fits that are different for each sample. The $R_1^{\text{Fe-Zr}}$ values for $\text{Fe}_{0.93}\text{Zr}_{0.07}$ and $\text{Fe}_{0.90}\text{Zr}_{0.10}$ were fixed to those reported in Table 2 (written here in italic). The Fe-film data are fitted with a BCC structure in the range $R = 1.8\text{--}4.9$ \AA (non-phase corrected) using a Hanning window.

lower contributions from the Fe-Zr paths, the $R_1^{\text{Fe-Zr}}$ distances were taken from the Gaussian fits. Allowing the radial distances of the second path R_2/R_1 to vary, did not really improve the quality of the fit for either Fe-Fe or for Fe-Zr. The values were therefore taken from the Gaussian fits of the simulated partial RDFs. For the $R_1^{\text{Fe-Fe}}$ values, the fitted and simulated values are very close for $\text{Fe}_{0.93}\text{Zr}_{0.07}$. However, as the Zr concentration increases, the simulated $R_1^{\text{Fe-Fe}}$ distance decreases, while the EXAFS fitted $R_1^{\text{Fe-Fe}}$ distance increases (see Fig. S3 in the Supplementary Information). The trend of increasing Fe-Fe distance with increasing Zr content agrees with the magnetic properties; The Curie temperature increases with increasing Zr content for the $\text{Fe}_{(1-x)}\text{Zr}_x$ samples (see

	From $g(r)$		EXAFS fit	
	Fe-Fe	Fe-Zr	Fe-Fe	Fe-Zr
R_2/R_1	1.08(2)	1.07(3)	<i>1.08</i>	<i>1.07</i>
σ_1^2/R_1^2	0.0018(3)	0.0017(6)	0.0016(2)	
σ_2^2/R_1^2	0.0045(20)	0.0035(21)	0.0014(7)	
N_1/c_B	6.4(8)	4.7(2.9)	8(1)	11(2)
$(N_1 + N_2)/c_B$	10.4(0.8)	13.3(1.0)	<i>10.4</i>	<i>13.3</i>

Table 5. Scaled parameters used in the EXAFS fits that are common for all compositions. The actual parameters that are used in the EXAFS paths (R_2 , σ_1^2 , σ_2^2 , N_1 , and N_2) are different for all concentrations since they are scaled by either R_1^{A-B} or the B atom content (c_B). The errorbars are estimated from the compositional variations. The parameter values are obtained from the fitting to the experimental EXAFS data except those written in italic that were fixed to the value obtained in the Gaussian fitting of the simulated partial radial distribution functions, $g(r)$.

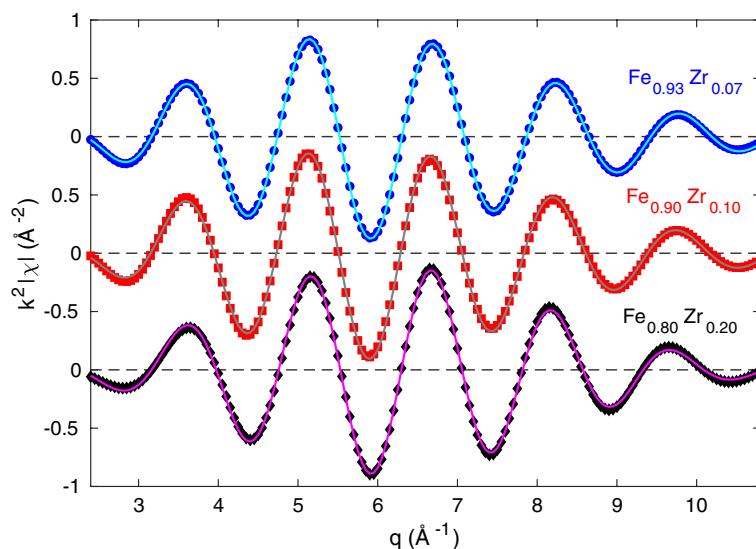


Figure 6. k^2 -weighted real part of $\chi(q)$ for experimental data (points) measured at 80 K and fits according to the four path model described in the text (lines). Both the experimental data and the fits are limited to the first shell. The back-Fourier analysis is made for $R \sim 1.5\text{--}2.7$ Å using a Hanning window for the experimental data (corresponding to non-phase corrected distances). The data are shifted for clarity with the dashed lines indicating each zero level.

Table S2 in the Supplementary Information) and a higher Curie temperature is related to a larger Fe-Fe distance according to the Bethe-Slater curve²⁰.

To summarise, the Fe-Fe distances are the biggest source of discrepancy between the simulated and real amorphous structures, a difference that increases with increasing Zr content. Due to the low Zr content, we cannot draw any conclusions about the Fe-Zr distances. We only note that the uncertainties are of the same order as the discrepancies in Fe-Fe distances. The two-path approach is a simple way of obtaining an asymmetric distribution of bond-lengths. Allowing N_1/c_B to vary while keeping both the R_2/R_1 ratios as well as the total coordination numbers fixed allow to modify this asymmetry without making the fitting procedure unstable. The coordination numbers scaled by the atomic content are in principle allowed to vary indirectly for each samples since the amplitude factors S_0^2 are fitted individually. However, the fitted S_0^2 values are within the uncertainties the same for all samples.

Coordination numbers. The Fe-Fe and Fe-Zr partial coordination numbers in the EXAFS fits are obtained by summing up those of the two paths and correcting for S_0^2 . These values are reported in Table 6 and compared to the coordination numbers obtained from the simulated structures using three different methods: (i) summing up those of the Gaussians with $i = 1$ and 2 obtained according to Eq. (2), (ii) from the partial RDF as

$$N^{A-B} = 4\pi\rho_B \int_0^{r_{\min}} r^2 g(r) dr, \quad (3)$$

		EXAFS fit	Equation (2)	Equation (3)	Voronoi
$N^{\text{Fe-Fe}}$	Fe _{0.93} Zr _{0.07}	7(2)	9.6(1)	10.5(3)	11.9(4)
	Fe _{0.90} Zr _{0.10}	8(2)	9.3(3)	10.0(2)	11.2(4)
	Fe _{0.80} Zr _{0.20}	7(2)	7.7(2)	8.3(2)	9.1(4)
$N^{\text{Fe-Zr}}$	Fe _{0.93} Zr _{0.07}	0.7(2)	0.9(2)	1.2(1)	1.3(1)
	Fe _{0.90} Zr _{0.10}	1.1(3)	1.3(1)	1.8(1)	1.8(1)
	Fe _{0.80} Zr _{0.20}	2.2(5)	2.5(3)	3.3(1)	3.4(1)
$N^{\text{Zr-Zr}}$	Fe _{0.93} Zr _{0.07}			1.5(1)	1.6(2)
	Fe _{0.90} Zr _{0.10}			2.1(2)	2.2(2)
	Fe _{0.80} Zr _{0.20}			4.1(3)	4.3(3)

Table 6. Nearest-neighbour coordination numbers obtained from the fitting of the EXAFS data and from the simulated structures. The coordination numbers of the simulated structures are calculated in three different ways: by summing N_1^{A-B} and N_2^{A-B} calculated from Eq. (2), from Eq. (3), and from a Voronoi analysis. Details about the distribution of Voronoi coordination numbers are presented in Fig. S4 in the Supplementary Information.

where the upper limit of the integral is the radial distance r_{\min} corresponding to the minimum in $g(r)$, and (iii) from a Voronoi analysis. Somewhat different coordination numbers are obtained with the different methods. It is, however, not surprising that lower coordination numbers are obtained from the Gaussians with $i = 1$ and 2 (Eq. 2) compared to integrating the partial RDFs up to r_{\min} (Eq. 3) if one looks at Fig. 2, where the limit of the first shell (r_{\min}/R_1) is indicated with a gray line. Due to the difference in obtained values depending on the method, the large uncertainties, and the known difficulty to obtain accurate coordination number of amorphous compounds from EXAFS data, we cannot state a significant discrepancy between the simulated and experimental coordination numbers.

Discussion

While many investigations of amorphous structures are based on independent theoretical or experimental observations, this work provides a detailed structural analysis of Fe-based amorphous alloys combining the theoretical information obtained by the computationally convenient SQ simulation method and the information extracted with an advanced fitting process from experimental EXAFS data. The simulation-enhanced fitting model surpasses the limitation of conventional EXAFS fitting and allows us to predict the compositional dependence of the magnetic properties for the investigated samples. At the same time, the results provide further confirmation of the validity of the SQ approach. Nonetheless, while we have found overall very good agreement between simulation and experiment, there are some discrepancies, accentuated by increasing the Zr content. One potential explanation is that in the sputtered samples, the Fe atoms might tend to be inhomogeneously distributed, as previously reported for Fe_(1-x)Zr_x samples with high Zr content^{23,29,30}. We note that this inhomogeneity is not the same as the formation of crystallites. It is rather a small deviation from the "most random" or most homogeneous amorphous structure due to the kinetics of the sputtered atoms and differences in glass forming ability with Zr-content. In the simulations, due to the nature of the stochastic quenching method, we rather expect a quite homogeneous amorphous structure independent of Zr-content. A second potential explanation, that we cannot exclude, is that the employed density functional theory implementation possesses some inherent quality differences between the pseudopotentials for Fe and Zr, causing the electron density distribution around Zr atoms to be slightly less accurate than that for Fe. These two hypotheses deserve further attention and indicate areas of improvement for simulations of real amorphous systems. However, this does not undermine the general validity of the simulation-enhanced fitting approach here proposed, and it does not prevent its application to other amorphous alloys, in particular in the case of low-concentration of the glassy former. This is also the most technologically relevant case at least for Fe-based amorphous soft-magnetic alloys.

Conclusions

To shed light on the complex structure of amorphous metals, a combination of theoretical modelling and experimental characterisation was used to study amorphous Fe_(1-x)Zr_x with $x = 0.07, 0.10$, and 0.20 . The partial radial distribution functions of the simulated atomic structures were used to create a model to simultaneously fit the experimental EXAFS data of all three samples to have a simple but accurate description of the atomic structures valid for any composition in the range $x = 0.07-0.20$ using a minimal number of free parameters. This approach allowed to extend the investigation beyond the individual limits of the theoretical model and the experimental data, revealing details of the structure not easily accessible. The EXAFS fitting revealed that the trend of the simulations of a slightly decreasing $R_1^{\text{Fe-Fe}}$ with increasing Zr content is incorrect and that in fact, $R_1^{\text{Fe-Fe}}$ increases slightly with increasing Zr content. The magnetic properties are highly sensitive to the nearest-neighbour Fe-Fe distances and the increase of Curie temperature with increasing Zr content is consistent with an increase in $R_1^{\text{Fe-Fe}}$ according to the Bethe-Slater curve²⁰.

A detailed amorphous structural description with accurate inter-atomic distances is a prerequisite for first-principles predictions of electronic and magnetic properties. The process outlined in this work can be generalised to other amorphous systems and is well suited also for multi-component glasses since the knowledge about the

simulated structures is used to reduce the complexity and the number of parameters included in the fitting of the experimental EXAFS data. Further combined experimental and atomic simulation studies could therefore pave the way for detailed investigations of the relationship between amorphous structures and physical properties. Such knowledge about the structure-properties relationship would be a valuable guide in the development of new amorphous materials with tailored functional properties.

Data availability

Request for any data should be addressed to the corresponding author (P.E.J.).

Received: 18 August 2022; Accepted: 21 March 2023

Published online: 27 March 2023

References

- Zallen, R. *The Physics of Amorphous Solids* (A Wiley-Interscience Publication, Wiley, 1998).
- Cheng, Y. Q. & Ma, E. Atomic-level structure and structure-property relationship in metallic glasses. *Prog. Mater. Sci.* **56**, 379–473. <https://doi.org/10.1016/j.pmatsci.2010.12.002> (2011).
- Dubois, J. M. & Le Caer, G. Ordre local et proprietes physiques des verres metalliques riches en fer. *Acta Metall.* **32**, 2101–2114. [https://doi.org/10.1016/0001-6160\(84\)90189-5](https://doi.org/10.1016/0001-6160(84)90189-5) (1984).
- Miracle, D. B. A structural model for metallic glasses. *Nat. Mater.* **3**, 697–702. <https://doi.org/10.1038/nmat1219> (2004).
- Hirata, A. *et al.* Direct observation of local atomic order in a metallic glass. *Nat. Mater.* **10**, 28–33. <https://doi.org/10.1038/nmat897> (2011).
- Hirata, A. *et al.* Geometric frustration of icosahedron in metallic glasses. *Science* **341**, 376–379. <https://doi.org/10.1126/science.1232450> (2013).
- Holmström, E. *et al.* Structure discovery for metallic glasses using stochastic quenching. *Phys. Rev. B* **82**, 024203. <https://doi.org/10.1103/PhysRevB.82.024203> (2010).
- Bock, N. *et al.* Liquid-state properties from first-principles density functional theory calculations: Static properties. *Phys. Rev. B* **82**, 144101. <https://doi.org/10.1103/PhysRevB.82.144101> (2010).
- Kádas, K. *et al.* Structural properties of amorphous metal carbides: Theory and experiment. *Acta Mater.* **60**, 4720–4728. <https://doi.org/10.1016/j.actamat.2012.04.044> (2012).
- Kresse, G. & Hafner, J. Ab initio molecular dynamics for liquid metals. *Phys. Rev. B* **47**, 558–561. <https://doi.org/10.1103/PhysRevB.47.558> (1993).
- Voloshin, V. P. & Naberukhin, Y. I. On the origin of the splitting of the second maximum in the radial distribution function of amorphous solids. *J. Struct. Chem.* **38**, 62–70. <https://doi.org/10.1007/BF02768808> (1997).
- Luo, W. K., Sheng, H. W. & Ma, E. Pair correlation functions and structural building schemes in amorphous alloys. *Appl. Phys. Lett.* **89**, 131927. <https://doi.org/10.1063/1.2356473> (2006).
- Pan, S. P., Qin, J. Y., Wang, W. M. & Gu, T. K. Origin of splitting of the second peak in the pair-distribution function for metallic glasses. *Phys. Rev. B* **84**, 092201. <https://doi.org/10.1103/PhysRevB.84.092201> (2011).
- Zhao, Y., Lin, D., Chen, X., Liu, Z. & Hui, X. Sluggish mobility and strong icosahedral ordering in Mg-Zn-Ca liquid and glassy alloys. *Acta Mater.* **67**, 266–277. <https://doi.org/10.1016/j.actamat.2013.12.037> (2014).
- Ding, J., Ma, E., Asta, M. & Ritchie, R. O. Second-nearest-neighbor correlations from connection of atomic packing motifs in metallic glasses and liquids. *Sci. Rep.* **5**, 17429. <https://doi.org/10.1038/srep17429> (2015).
- Bennett, C. H. Serially deposited amorphous aggregates of hard spheres. *J. Appl. Phys.* **43**, 2727–2734. <https://doi.org/10.1063/1.1661585> (1972).
- Olovsson, W., Alling, B. & Magnuson, M. Structure and bonding in amorphous Cr_{1-x}C_x nanocomposite thin films: X-ray absorption spectra and first-principles calculations. *J. Phys. Chem. C* **120**, 12890–12899. <https://doi.org/10.1021/acs.jpcc.6b03608> (2016).
- George, S. *et al.* Local structure in amorphous Sm_xCo_{1-x}: A combined experimental and theoretical study. *J. Mater. Sci.* **55**, 12488–12498. <https://doi.org/10.1007/s10853-020-04848-4> (2020).
- Inoue, A. & Takeuchi, A. Recent development and applications of bulk glassy alloys. *Int. J. Appl. Glas. Sci.* **1**, 273–295. <https://doi.org/10.1111/j.2041-1294.2010.00019.x> (2010).
- McHenry, M. E., Willard, M. A. & Laughlin, D. E. Amorphous and nanocrystalline materials for applications as soft magnets. *Prog. Mater. Sci.* **44**, 291–433. [https://doi.org/10.1016/S0079-6425\(99\)00002-X](https://doi.org/10.1016/S0079-6425(99)00002-X) (1999).
- Barandiarán, J. *et al.* Tensile stress dependence of the Curie temperature and hyperfine field in Fe-Zr-B-(Cu) amorphous alloys. *Phys. Rev. B Condens. Matter Mater. Phys.* **54**, 3026–3029. <https://doi.org/10.1103/PhysRevB.54.3026> (1996).
- Ryan, D. H., Coey, J. M. D., Batalla, E., Altounian, Z. & Ström-Olsen, J. O. Magnetic properties of iron-rich Fe-Zr glasses. *Phys. Rev. B* **35**, 8630–8638. <https://doi.org/10.1103/PhysRevB.35.8630> (1987).
- El Hafidi, M., Chouteau, G., Béthoux, O. & Sadoc, A. Transition from the non-magnetic to the magnetic state in Zr_{1-x}Fe_x sputtered amorphous alloys. *J. Magn. Magn. Mater.* **81**, 1–13. [https://doi.org/10.1016/0304-8853\(89\)90222-9](https://doi.org/10.1016/0304-8853(89)90222-9) (1989).
- Kaul, S. N., Siruguri, V. & Chandra, G. Magnetization and Mössbauer study of the reentrant amorphous Fe₉₀Zr₁₀ alloy. *Phys. Rev. B* **45**, 12343–12356. <https://doi.org/10.1103/PhysRevB.45.12343> (1992).
- Van Lierop, J. & Ryan, D. H. Spin dynamics in a frustrated magnet. *Phys. Rev. Lett.* **86**, 4390–4393. <https://doi.org/10.1103/PhysRevLett.86.4390> (2001).
- Wildes, A. R. *et al.* The magnetic structures of some Fe_{100-x}Zr_x metallic glasses. *J. Phys. Condens. Matter* **15**, 675–691. <https://doi.org/10.1088/0953-8984/15/4/308> (2003).
- Calderón, R. G. *et al.* Small-angle neutron scattering study of a magnetically inhomogeneous amorphous alloy with reentrant behavior. *Phys. Rev. B Condens. Matter Mater. Phys.* **71**, 134413. <https://doi.org/10.1103/PhysRevB.71.134413> (2005).
- Sharma, P., Kimura, H. & Inoue, A. Magnetic behavior of cosputtered Fe-Zr amorphous thin films exhibiting perpendicular magnetic anisotropy. *Phys. Rev. B Condens. Matter Mater. Phys.* **78**, 134414. <https://doi.org/10.1103/PhysRevB.78.134414> (2008).
- Kim, M., Sung, N. E. & Lim, S. H. Large variation of magnetic properties of amorphous Fe-Zr thin films with Ar pressure during sputtering. *Sci. Rep.* **7**, 41894. <https://doi.org/10.1038/srep41894> (2017).
- Kim, M. & Lim, S. H. Magnetic behavior of amorphous Fe-Zr thin films sputtered at different Ar pressures. *J. Magn. Magn. Mater.* **476**, 559–567. <https://doi.org/10.1016/j.jmmm.2019.01.030> (2019).
- Korelis, P. T. T. *et al.* Highly amorphous Fe₉₀Zr₁₀ thin films, and the influence of crystallites on the magnetism. *Thin Solid Films* **519**, 404–409. <https://doi.org/10.1016/j.tsf.2010.07.084> (2010).
- Zamani, A. *et al.* Magnetic properties of amorphous Fe₉₃Zr₇ films: Effect of light ion implantation. *J. Appl. Phys.* **117**, 143903. <https://doi.org/10.1063/1.4917212> (2015).
- Mayer, M. SIMNRA, a simulation program for the analysis of NRA. In *RBS and ERDA. AIP Conf. Proc.* vol 475, 541–544. <https://doi.org/10.1063/1.59188> (1999).

34. Mayer, M. Improved physics in SIMNRA 7. *Nucl. Instruments Methods Phys. Res. Sect. B Beam Interact. Mater. Atoms* **332**, 176–180. <https://doi.org/10.1016/j.nimb.2014.02.056> (2014).
35. Björck, M. & Andersson, G. GenX: An extensible X-ray reflectivity refinement program utilizing differential evolution. *J. Appl. Crystallogr.* **40**, 1174–1178. <https://doi.org/10.1107/S0021889807045086> (2007).
36. Krompiewski, S., Krauss, U. & Krey, U. Computer studies of magnetization for amorphous fe_{1-x}zrx alloys. *Phys. Rev. B* **39**, 2819–2821. <https://doi.org/10.1103/PhysRevB.39.2819> (1989).
37. Bakonyi, I. Atomic volumes and local structure of metallic glasses. *Acta Mater.* **53**, 2509–2520. <https://doi.org/10.1016/j.actamat.2005.02.016> (2005).
38. Ravel, B. & Newville, M. ATHENA, ARTEMIS, HEPHAESTUS: Data analysis for X-ray absorption spectroscopy using IFEFFIT. *J. Synchrotron Radiat.* **12**, 537–541. <https://doi.org/10.1107/S0909049505012719> (2005).
39. Kresse, G. & Hafner, J. Ab initio molecular-dynamics simulation of the liquid-metalamorphous- semiconductor transition in germanium. *Phys. Rev. B* **49**, 14251–14269. <https://doi.org/10.1103/PhysRevB.49.14251> (1994).
40. Kresse, G. & Furthmüller, J. Efficiency of ab-initio total energy calculations for metals and semiconductors using a plane-wave basis set. *Comput. Mater. Sci.* **6**, 15–50. [https://doi.org/10.1016/0927-0256\(96\)00008-0](https://doi.org/10.1016/0927-0256(96)00008-0) (1996).
41. Kresse, G. & Furthmüller, J. Efficient iterative schemes for ab initio total-energy calculations using a plane-wave basis set. *Phys. Rev. B Condens. Matter Mater. Phys.* **54**, 11169–11186. <https://doi.org/10.1103/PhysRevB.54.11169> (1996).
42. Kresse, G. & Joubert, D. From ultrasoft pseudopotentials to the projector augmented-wave method. *Phys. Rev. B* **59**, 1758–1775. <https://doi.org/10.1103/PhysRevB.59.1758> (1999).
43. Blöchl, P. E. Projector augmented-wave method. *Phys. Rev. B* **50**, 17953–17979. <https://doi.org/10.1103/PhysRevB.50.17953> (1994).
44. Perdew, J. P., Burke, K. & Ernzerhof, M. Generalized gradient approximation made simple. *Phys. Rev. Lett.* **77**, 3865–3868. <https://doi.org/10.1103/PhysRevLett.77.3865> (1996).
45. Perdew, J. P., Burke, K. & Ernzerhof, M. Generalized gradient approximation made simple [Phys. Rev. Lett. 77, 3865 (1996)]. *Phys. Rev. Lett.* **78**, 1396–1396. <https://doi.org/10.1103/PhysRevLett.78.1396> (1997).
46. Hohenberg, P. & Kohn, W. Inhomogeneous electron gas. *Phys. Rev.* **136**, B864–B871. <https://doi.org/10.1103/PhysRev.136.B864> (1964).
47. Kohn, W. & Sham, L. J. Self-consistent equations including exchange and correlation effects. *Phys. Rev.* **140**, A1133–A1138. <https://doi.org/10.1103/PhysRev.140.A1133> (1965).
48. Rycroft, C. H. Voronoi++: A three-dimensional voronoi cell library in c++. *Chaos Interdiscip. J. Nonlinear Sci.* **19**, 041111. <https://doi.org/10.1063/1.3215722> (2009).
49. Rehr, J. J. *et al.* Ab initio theory and calculations of X-ray spectra. *Comptes Rendus Phys.* **10**, 548–559. <https://doi.org/10.1016/j.crhy.2008.08.004> (2009).
50. Rehr, J. J. & Albers, R. C. Theoretical approaches to x-ray absorption fine structure. *Rev. Mod. Phys.* **72**, 621–654. <https://doi.org/10.1103/RevModPhys.72.621> (2000).

Acknowledgements

Financial support from the Swedish Research Council (VR) is gratefully acknowledged. R.H.S thanks VR grant 2017-04627, and P.E.J thanks VR grant 2014-05951. The computations were enabled by resources provided by the Swedish National Infrastructure for Computing (SNIC) at the National Supercomputer Centre at Linköping University. The authors thank S. Carlson for assistance during the experiments at MAX-lab and Gabriella Andersson, Olle Eriksson, Björgvin Hjörvarsson, and Krisztina Kádas for helpful discussions.

Author contributions

R.J., R.A., and R.H.S. designed the research for the computational simulations; R.J. performed the simulations. G.M., M.A., and P.E.J. designed the experimental research with input from D.A.; G.M., S.G., and M.A. conducted the experiments with input from P.E.J and D.A; G.M., R.J, R.H.S, and P.E.J. analysed and interpreted the data and wrote the manuscript with input from all co-authors.

Funding

Open access funding provided by Uppsala University.

Competing interests

The authors declare no competing interests.

Additional information

Supplementary Information The online version contains supplementary material available at <https://doi.org/10.1038/s41598-023-32051-3>.

Correspondence and requests for materials should be addressed to P.E.J.

Reprints and permissions information is available at www.nature.com/reprints.

Publisher's note Springer Nature remains neutral with regard to jurisdictional claims in published maps and institutional affiliations.



Open Access This article is licensed under a Creative Commons Attribution 4.0 International License, which permits use, sharing, adaptation, distribution and reproduction in any medium or format, as long as you give appropriate credit to the original author(s) and the source, provide a link to the Creative Commons licence, and indicate if changes were made. The images or other third party material in this article are included in the article's Creative Commons licence, unless indicated otherwise in a credit line to the material. If material is not included in the article's Creative Commons licence and your intended use is not permitted by statutory regulation or exceeds the permitted use, you will need to obtain permission directly from the copyright holder. To view a copy of this licence, visit <http://creativecommons.org/licenses/by/4.0/>.

© The Author(s) 2023